ORIGINAL ARTICLE

**Thomas Boeck · Jie Li · Enrique López-Pagés ·
Philip Yecko · Stéphane Zaleski**

Ligament formation in sheared liquid–gas layers

Abstract We perform numerical simulations of two-phase liquid–gas sheared layers, with the objective of studying atomization. The Navier–Stokes equations for two-dimensional incompressible flow are solved in a periodic domain. A volume-of-fluid method is used to track the interface. The density ratio is kept around 10. The calculations show good agreement with a fully viscous Orr–Sommerfeld linear theory over several orders of magnitude of interface growth. The nonlinear development shows the growth of finger-like structures, or ligaments, and the detachment of droplets. The effect of the Weber and Reynolds numbers, the boundary layer width and the initial perturbation amplitude are discussed through a number of typical cases. Inversion of the liquid boundary layer is shown to yield more readily ligaments bending upwards and is thus more likely to produce droplets.

Keywords Kelvin-Helmholtz instability · Two-fluid mixing layer · Atomization · Multiphase shear flow · Ligaments · Droplet formation · Ligament breakup · Volume of fluid

PACS 47.55.Ca, 47.55.db, 47.55.df

1 Introduction

A strong gas flow parallel to a liquid–gas interface tends to shatter it into small droplets. Wind, when of sufficient magnitude, will strip droplets from wave crests. Many industrial atomization processes rely on the atomization of fast liquid jets into droplets. This spray-formation process is of considerable importance in combustion technology. A case in point is air-blast atomization devices [21] or coaxial injectors in cryogenic engines.

Communicated by J. R. Blake.

T. Boeck
Fachgebiet Thermo- und Fluiddynamik, TU Ilmenau, P.O. Box 100565, 98684 Ilmenau, Germany

J. Li
Department of Engineering, University of Cambridge, Trumpington Street, Cambridge CB2 1PZ, UK

E. López-Pagés
Fluid Mechanics Department, Universidad de Zaragoza, Zaragoza 50015, Spain

P. Yecko
Department of Mathematical Sciences, Montclair State University, Montclair, NJ 07043, USA

S. Zaleski (✉)
Laboratoire de Modélisation en Mécanique, CNRS and Université Pierre et Marie Curie (Paris VI),
4 Place Jussieu, Paris 75005, France
E-mail: zaleski@lmm.jussieu.fr

Our current understanding of the mechanisms leading to atomization rests in part on various theoretical approaches and in part on experimental observation. In addition there are relatively few numerical studies [20, 29,30]. The work reported here focuses on the influence of viscosity on ligament formation and sizes. Various mechanisms have been suggested to explain liquid jet atomization [19,26]. At sufficiently low Weber number (defined below) the Savart–Plateau–Rayleigh jet instability dominates and creates droplets of roughly the size of the jet. At larger velocities, instabilities of much shorter length scale develop.

At these large speeds, the process is rather complex. It involves turbulence upstream of the injector, as argued by Faeth et al.[8], instabilities near the injector due to the shearing motion of the liquid and the gas, ligament and droplet formation and dispersion in an initially dense spray. The region near the nozzle, where spray formation is initiated by the growth of surface instabilities, is thus especially interesting. To understand the instabilities that develop in this region we focus in this paper on the two-dimensional, spatially periodic shear flow. This simplification is warranted by the approximately periodic nature of the flow observed in experiments (see for instance [16,19]).

There is a large amount of literature on the linear theory of the instability. The classical stability theory of Chandrasekhar [6] predicts droplet formation when the gas Weber number We (defined below) exceeds a critical value. One other effect of viscosity is to impose the existence of a critical Reynolds number for instability development. Recently, we have discussed [33] the full viscous stability theory, finding several distinct modes of instability. In contrast, relatively little work can be found on the nonlinear development. The inviscid fluid equations were solved by Rangel and Sirignano [24] using a boundary-integral method for moderate density ratios $r = \rho_g/\rho_l$, however despite the large Reynolds numbers at which atomization occurs, it is likely that finite viscosity effects are present and thus inviscid fluid flow may not be close to the Navier–Stokes solutions.

Full simulations of the Navier–Stokes equations for two-phase liquid–gas layers have seldom been performed. Our group has performed calculations using volume-of-fluid (VOF) methods. Some preliminary two-dimensional results may be found in Keller et al. [17], Li [22] and Leboissetier and Zaleski [20] , while Zaleski et al. [34,35] and Bianchi et al. [2] have shown some preliminary three-dimensional (3D) results. Agreement between the volume-of-fluid calculations and linear theory is particularly difficult to obtain because of the complex effect of viscosity on the base profile and on the instability growth rates and modes. Recently two- and three-dimensional solutions of the full Navier–Stokes equations have been performed by interface tracking methods, using connected markers to follow the interface [29,30].

In this paper we focus on the effect of viscosity on the length scales of the ligaments and droplets. The theories existing today for droplet size (see [19] for a review and [23] for recent results) all assume that the droplet size is proportional to the wavelength of the instability. However in this paper we fix the wavelength of the instability and observe the variation in droplet sizes. This should lead to improved theories for droplet formation.

2 Basic equations and numerical method

We model the problem assuming sharp interfaces between two Newtonian, viscous fluids with constant surface tension, in two dimensions of space. This leads to the Navier–Stokes equations. We note $\mathbf{u}(\mathbf{x}, t)$, $p(\mathbf{x}, t)$ the velocity and pressure field, σ the surface tension (assumed constant), κ the interface curvature, $\mathbf{n}$ the normal to the interface, μ the viscosity. The equations are

$$\partial_t \mathbf{u} + \mathbf{u} \cdot \nabla \mathbf{u} = -\frac{1}{\rho} \nabla p + \frac{1}{\rho} \nabla \cdot (2\mu \mathbf{D}) + \sigma \kappa \mathbf{n} \delta_S, \tag{1}$$

where δ_S is a distribution concentrated on the interface and $\mathbf{D}$ is the rate-of-strain tensor

$$D_{ij} = \frac{1}{2} \left(\frac{\partial u_j}{\partial x_i} + \frac{\partial u_i}{\partial x_j} \right). \tag{2}$$
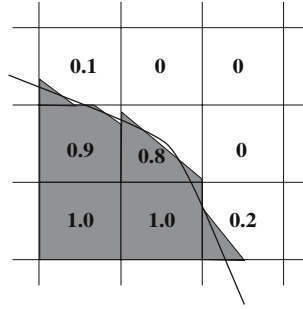
Incompressible flow is assumed

$$\nabla \cdot \mathbf{u} = 0. \tag{3}$$

The interface follows the flow, or in other words, the normal velocity of the interface equals the normal flow velocity $\mathbf{u} \cdot \mathbf{n}$. For an interface height $h(x, t)$ this implies

$$\partial_t h = v - u \partial_x h \tag{4}$$

The viscosity and density are constant in each phase but vary from phase to phase. An important consequence of Eq. (1) are the jump conditions on the interface:

Fig. 1 The basic principle of the VOF piecewise linear interface calculation (PLIC) method: the interface is reconstructed by linear unconnected segments in each cell

$$[\mathbf{u}]_S = 0 \tag{5}$$

for the velocity, and

$$[-p\mathbf{n} + 2\mu\mathbf{n} \cdot \mathbf{D}]_s = \sigma\kappa\mathbf{n}, \tag{6}$$

for the stress.

These equations are solved in a square $L \times L$ domain and periodic boundary conditions are used in the x direction. In the y-direction we use free-slip boundary conditions so that $v = 0$ and $\partial_y u = 0$. To specify the problem fully we also need initial conditions. The initial base flow is described in Sects. 3 and 4. To this base flow we add an initial perturbation $\epsilon\mathbf{u}_1(\mathbf{x}, 0)$ where ϵ is some small number.

With periodic boundary conditions, the problem is invariant under any Galilean transformation that shifts the horizontal velocity field. Thus the only relevant velocity scale is the velocity difference ΔU. With the above parameters several dimensionless numbers may be defined, such as the Weber numbers $\text{We}_i = \rho_i(\Delta U)^2 L/\sigma$ based on the gas ($i = \text{g}$) or the liquid ($i = \text{l}$) and similarly the Reynolds numbers $\text{Re}_i = \rho_i \Delta U L/\mu_i$. Two additional numbers are the density and viscosity ratios $r = \rho_\text{g}/\rho_\text{l} = \text{We}_\text{g}/\text{We}_\text{l}$ and $k = \nu_\text{g}/\nu_\text{l} = \text{Re}_\text{l}/\text{Re}_\text{g}$. With, for instance, We_g, Re_g, r and k we have a full set of parameters. For convenience we will also refer to $m = \mu_\text{g}/\mu_\ell$.

We solve these equations using a combination of numerical methods described in several prior publications [11,18,22,27]. The flow in the gas and liquid is considered as the flow of a single fluid with variable viscosity and density, and with singular forces inside the domain, in a manner consistent with the formulation used in Eq. (1). We then discretize directly Eq. (1) on a square, staggered, finite-difference grid known as the marker-and-cell (MAC) grid. An explicit projection method is used for the pressure. This method requires the resolution of an elliptic equation for the pressure, which is solved using a multigrid method. The multigrid resolution is made more efficient by tuning the number of iterations of the smoothing operator. The tuning is a function of the convergence rate.

The motion of the interface following the flow is tracked using a second-order VOF method described in Li [22]; Gueyffier et al. [11]. The interface is located by a VOF function C_{ij}, and is reconstructed at each time step as a series of linear segments (Fig. 1). The principal advantage of this method compared to its competition is that it ensures very good volume conservation. To transport the interface segments from cell to cell we use the *explicit Lagrangian* method (see Li [22]; Scardovelli and Zaleski [28]; Aulisa et al. [1]), which conserves mass with acceptable accuracy (better that 0.1%) and automatically breaks thin ligaments.

For the viscosity of mixed cells we used two methods. The first method is the arithmetic mean

$$\mu_{ij} = \mu_1 C_{ij} + \mu_2(1 - C_{ij}), \tag{7}$$

where μ_p is the viscosity of phase p and μ_{ij} the viscosity at location ij. When the viscosity is needed at staggered grid locations averages of neighboring points are taken. The other method is the harmonic mean

$$\mu_{ij}^{-1} = \mu_1^{-1} C_{ij} + \mu_2^{-1}(1 - C_{ij}). \tag{8}$$

The arithmetic mean is optimal in a shear flow when the interface is perpendicular to the flow, while the harmonic mean is optimal when the interface is parallel to the flow.

Surface tension is also represented using an approximation of the distribution δ_S in (1) over the grid. We use the *continuous surface stress* formulation described in Lafaurie et al. [18] in which the surface tension force is represented in a continuous way. The normal is calculated by

$$\mathbf{n} = \frac{\nabla_h C}{||\nabla_h C||}, \tag{9}$$

where ∇_h is a finite-difference operator. To compute the capillary term we use the identity (valid for constant σ)

$$\sigma \kappa \mathbf{n} \delta_S = \nabla \cdot [\sigma (\mathbf{I} - \mathbf{n} \otimes \mathbf{n})]. \tag{10}$$

We discretize it using

$$\sigma \kappa \mathbf{n} \delta_S = \nabla_h \cdot [\sigma (\mathbf{1} - \mathbf{n}_h \otimes \mathbf{n}_h) ||\nabla_h C||] \tag{11}$$

In some cases (discussed below) we replace C by a smoothed field. In the smoothed version the function C_{ij} is filtered to obtain a smoothed function

$$\tilde{C}_{ij} = \frac{1}{2} C_{ij} + \frac{1}{8} [C_{i,j-1} + C_{i,j+1} + C_{i-1,j} + C_{i+1,j}], \tag{12}$$

which we then use in expressions (9) and (11). This representation of surface tension has been shown to give good results for small-amplitude capillary waves. Indeed, simulations and theory compare well for capillary surface oscillations as shown in Gueyffier et al. [11]. The smoothing is generally considered to be a useful operation as it reduces spurious currents [11] however we show in Sect. 4.5 that it may also have drawbacks.

3 Comparison with linear theory

Many previous tests of components of this code have been performed, but it has not been possible to successfully compare the instability growth with linear theory.

A specific test of our code for the study of sheared layers is to compare its predictions to those of the linear theory. Conversely, the linear theory is also tested. The linear theory is rather complex and has been worked out in detail only recently by Yecko et al. [33]; Boeck and Zaleski [3]; Gordillo and Perez-Saborid [10]. An important conclusion of the recent work is that great care must be taken to resolve the viscous stability problem with the corresponding Orr–Sommerfeld equations, since their growth rates are very different from the inviscid ones. In particular a new H-mode, named after Hooper and Hinch [12–15] was found at higher wavenumbers and growth rates than the previously known modes. Here we give only the result of the comparison between the linear theory and full numerics; for a discussion of the theory and modes the reader is referred to the above references.

The typical base flow takes some time to adapt after the nozzle exit but eventually settles to a flow with two boundary layers: one in the gas and the other in the liquid. A realistic base flow that is a solution of the Navier–Stokes equations has been considered (Fig. 2c). It is made of two error-function profiles with

$$u_{0,i}(y) = U_i \mathrm{erf}\left(\frac{y}{\delta_i}\right), \tag{13}$$

where the index $i = $ g for $y > 0$ and $i = $ l otherwise. When $\delta_i = \sqrt{4\nu_i(t + t_0)}$ this is the flow that would evolve from the step function profile at $t = -t_0$.

At $t = 0$ there are two boundary layers of size $\delta_i = \sqrt{4\nu_i t_0}$. Then

$$\frac{\delta_g}{\delta_l} = \sqrt{\frac{\nu_g}{\nu_l}}. \tag{14}$$

It is also useful to define numbers based on the boundary-layer size $\mathrm{Re}_g^\star = U_g \delta_g / \nu_g$ and $\mathrm{We}_g^\star = \rho_g U_g^2 \delta_g / \sigma$. The two boundary layers must satisfy the stress balance condition (6), which yields

$$\frac{\mu_g U_g}{\delta_g} = \frac{\mu_l |U_l|}{\delta_l} \tag{15}$$

Together with (14) this equation fixes the ratio U_g / U_l. For realistic liquid–gas parameter values one finds $U_g \gg |U_l|$. When the Reynolds numbers are large the boundary layers grow slowly by diffusion.

The full viscous Navier–Stokes equations were perturbed to find a linearized approximation. The resulting Orr–Sommerfeld equations were solved using a polynomial expansion and standard linear-algebra packages [3,33]. Comparison of the full numerical simulations with the predictions of the Orr–Sommerfeld theory gave
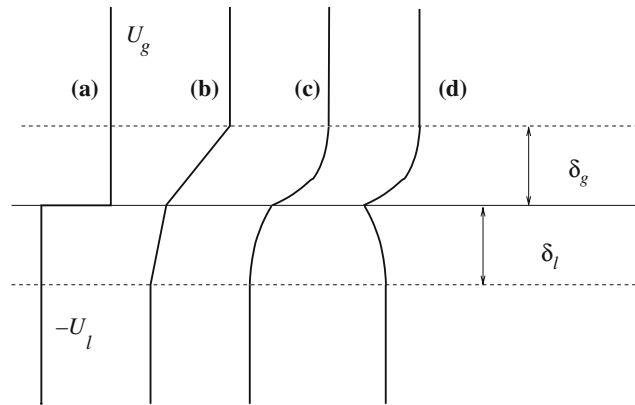
Fig. 2 The initial or base flows discussed in this paper: *a* The simplest profile: sharp velocity jump. *b* A piecewise linear flow with two boundary layers used in early studies. *c* A smooth boundary layers profile, used for comparisons with linear theory and in most full simulations. *d* An inverted liquid boundary layer, which mimics the situation just outside the nozzle
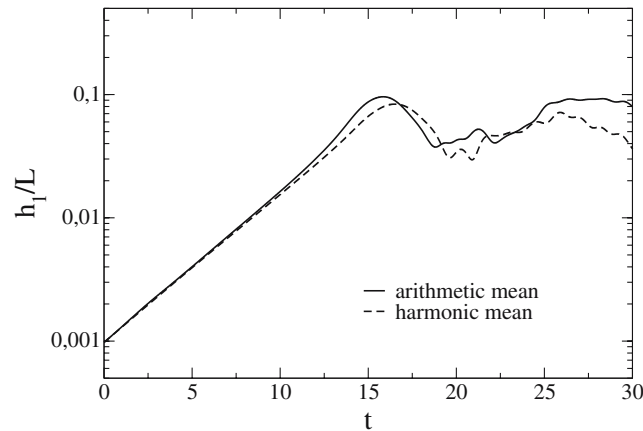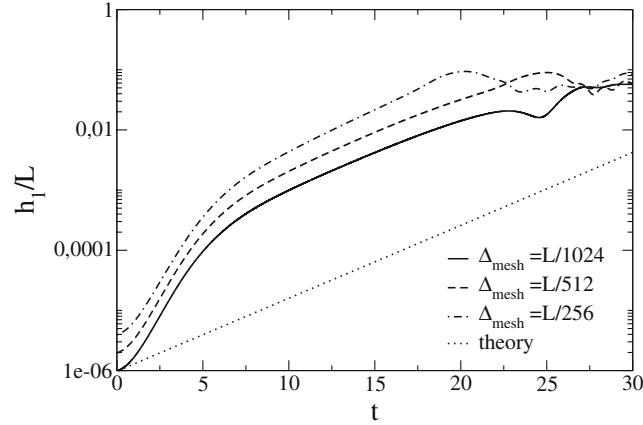

Fig. 3 Amplitude growth of the a perturbation with wavelength $\lambda = L$ for the arithmetic and harmonic mean of the viscosity. The initial amplitude equals half the mesh spacing. The numerically obtained amplitude growth is indistinguishable from the theoretical straight line obtained from the solution of the Orr–Sommerfeld equations in the early linear part. The Reynolds number is $Re_g = 8000$, boundary layer sizes are $\delta_g = \delta_1 = L/4$, density ratio is $r = 0.1$, viscosity ratio is $\mu_g/\mu_1 = 0.02$, meshsize is 512^2. Time is measured in units of $L/\Delta U$

excellent agreement, as shown in Fig. 3. The computations reported in this section were initialized using the linear mode computed from the Orr–Sommerfeld equation. Exponential growth was observed over a range of amplitudes of several orders of magnitude. Details of the analysis and numerical resolution of the linearized equations may be found in Yecko et al. [33], and Boeck and Zaleski [3].

Another delicate point when performing a comparison between linear theory and simulations is the need to avoid artifacts at early times. At initial time the flow is set to the mode given by linear theory. The correct growth rate is embedded in this mode: indeed the initial velocity of the fluid under the interface in that mode is $v_0 = dh/dt(0) = h_0 s$, where s is the growth rate and h_0 is the initial interface height. Thus the short-time dependence $h(t) = h_0 + h_0 st$ yields, still at short times, an apparent growth of the form $h = h_0 \exp(st)$. To avoid this type of artifact it is important to continue the simulation until h/h_0 has varied by several orders of magnitude, as we did in our comparisons. Moreover one of us (P.Y.) has also compared the full numerical solution starting from random initial perturbations, finding equally good agreement with Orr–Sommerfeld theory.

In Fig. 4 a typical comparison is shown. In this figure and the following ones, h_1 is the Fourier amplitude of the interface deformation $h(x)$ with the maximal wavelength L. The amplitude of the perturbation starts at 10^{-6}, much smaller than the grid spacing. To compare with the most commonly used method, we have used the arithmetic mean. The initial growth is faster than the theory, but as the amplitude reaches the level of the grid spacing, the numerical and theoretical growth rates agree. When one uses the harmonic mean, the initial

Fig. 4 Amplitude growth for an unstable mode as a function of dimensionless time. The parameters are as in Figure 3 except for the initial amplitude of the perturbation, which is a $1/1000$-fraction of the mesh spacing. The arithmetic mean and three different mesh spacings are used in the calculations. The theoretical curve omitted in Fig. 3 is shown for comparison.
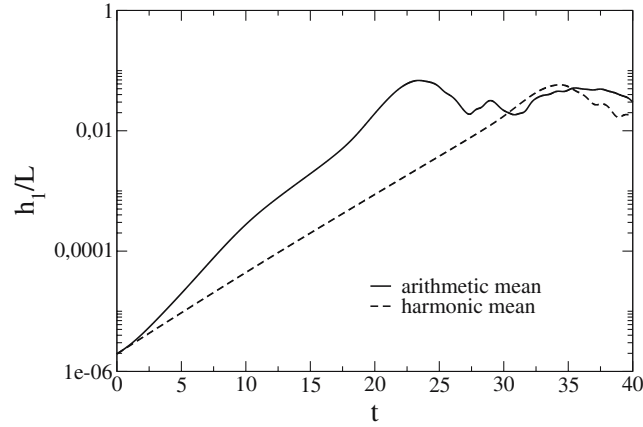
Fig. 5 Amplitude growth of the a perturbation with wavelength $\lambda = L$ for the arithmetic and harmonic mean of the viscosity. The initial amplitude equals $1/1000$ of the mesh spacing. The Reynolds number is $\text{Re}_g = 8000$, boundary layer sizes are $\delta_g = \delta_1 = L/4$, density ratio is $r = 0.1$, viscosity ratio is $\mu_g/\mu_1 = 0.1$, meshsize is 512^2. The result for harmonic mean is again indistinguishable from the theoretical straight line obtained from the solution of the Orr–Sommerfeld equations.
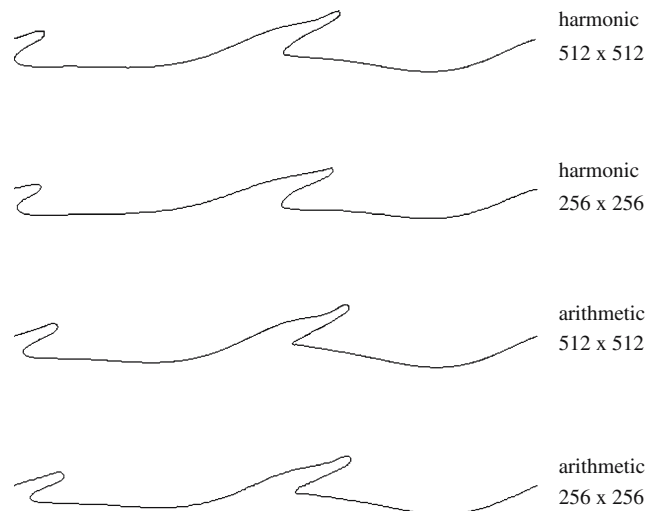
rapid-growth phase does not appear and the agreement with theory is immediate (Fig. 5). Finally when the initial amplitude of the perturbation is large enough, there is no difference between the two methods (Fig. 3).

There is a significant difference between the two methods, but it appears only when the deformations are smaller than the grid size. The harmonic mean is definitely preferred here, but we do not exclude that the arithmetic mean may be better in other flow configurations.

4 Nonlinear results

4.1 Initial conditions and simulation parameters

Initially, a liquid layer of thickness $L/3$ is placed at the bottom of a square $L \times L$ simulation domain, corresponding to an uniform square grid. The interface is flat at initial time while we used various profiles for the velocity. The instability is triggered by inserting two pairs of vortices inside the liquid phase. Therefore, the initial wavelength of the imposed instability is $\lambda = 0.5L$. The vortices are patches of uniform vorticity of radius $r_c = 4 \times 10^{-2}L$. Their dimensionless circulation (indicated in Table 1) is $\Gamma = (\oint u \mathrm{d}l)/(2\pi \Delta U L)$, where ΔU is the velocity difference between gas and liquid. For two boundary layers $\Delta U = U_g + U_1$. In what follows we use dimensionless numbers $\text{Re}_{1,g}$, $\text{We}_{1,g}$ based on ΔU and L.

harmonic
512 x 512

harmonic
256 x 256

arithmetic
512 x 512

arithmetic
256 x 256

Fig. 6 Nonlinear development of the instability for the two viscosity methods and two grid sizes (case D)

We have performed a very large number of simulations at various values of the parameters. There are however about eight independent parameters (the six shown in Table 1 and Re_1 and r). A full parametric study as a function of the eight parameters is beyond the means of the present study, so we had to fix the values of some of the parameters. The overall principle guiding the choice of the parameter is numerical convenience: it is difficult to perform accurate simulations when the surface tension (dimensionless surface tension may be measured by the Laplace number $La = \rho_l d\sigma/\mu_l^2 = Re_l^2/We_l$ where d is a characteristic length scale.), the Reynolds numbers and the density ratio are all large. Although such computations are not impossible, they are much more complex. The simulations in this paper are thus restricted to the case $r = 0.1$ which is simpler than the air–water one (which has $r \approx 0.0012$). This simpler case has however direct applications to liquid–gas atomization at high pressure. We let $Re_1 = 1,000$ as this provides a liquid viscosity low enough to diminish the effect of liquid viscosity on ligament formation. The other parameters varied are Re_g and We_g, and, in some cases, the boundary layer width and structure.

The initial boundary-layer configuration is delicate to fix. In all cases except D3 and E, the boundary layer widths are fixed by the diffusive growth condition (14). The ratio U_g/U_l is fixed by the stress-balance condition (15).

4.2 Convergence study

The effect of grid resolution is a difficult issue that we discuss in this section and in Sect. 4.8. In Fig. 6 we show the result of a comparison between the two viscosity methods (harmonic and arithmetic) and for two grid sizes. The parameters are those of case D in Table 1.

We see that convergence is attained in both cases, and that the choice of the viscosity method has no visible effect. On the other hand when we initialize the simulation with an initial sharp velocity profile as shown in Fig. 2a (a simplification used in most simulations of the literature) we see two effects in Fig. 7. One is that, as the grid is refined, increasingly small structures are seen. The other effect is that these small structures are more pronounced in the arithmetic-mean case. A likely explanation for the small structures is as follows: the case of a sharp velocity profile is essentially identical to a profile where the boundary layers have shrunk to the size of the grid spacing. As the boundary layers decrease in size, the modes found by the Orr–Sommerfeld theory [3] reach a very large growth rate and wavenumber. This can be seen by comparing Fig. 19 and Fig. 22 containing the growth rates for the cases D and D2. For the second effect, the growth is enhanced in the arithmetic mean case as it gives faster growth in the initial instants as in Fig. 4.
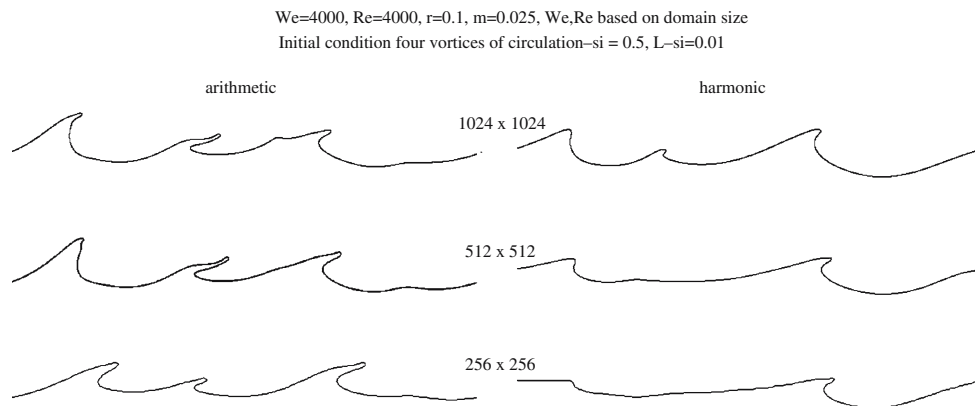
From these results, we conclude that the initial sharp velocity profile (Fig. 2a) is an ill-posed problem: ever-faster growth rates are obtained as the grid is refined and larger wavenumber are explored. Thus in what follows we always initialize the flow with small boundary layers in *both the gas and in the liquid*.

Table 1 Parameters used in the unequal density simulations.

Run	$\mathrm{Re}_{\mathrm{g}}(L)$	$\mathrm{We}_{\mathrm{g}}(L)$	$\mu_{\mathrm{g}}/\mu_{\mathrm{l}}$	δ_{g}/L	δ_{l}/L	Γ	$\mathrm{Re}_{\mathrm{g}}^{\star}$	$\mathrm{We}_{\mathrm{g}}^{\star}$
A	500	500	0.2	0.1	0.707	0.075	43.81	38.38
B	4,000	500	0.025	0.1	0.2	0.025	380.95	45.35
C	500	4,000	0.2	0.1	0.707	0.025	43.81	307.02
D	4,000	4,000	0.025	0.1	0.2	0.025	380.95	362.81
D1	4,000	4,000	0.025	0.1	0.2	0.05	380.95	362.81
D2	4,000	4,000	0.025	0.01	0.02	0.05	38.1	36.28
D3	4,000	4,000	0.025	0.1	Inverted b.l. (see text)			
E	4,000	4,000	0.025	None	None	0.025	–	–

None instead of a value for $\delta_{\mathrm{l,g}}/L$ means that there were no boundary layers (b.l.). Numbers $\mathrm{Re}_{\mathrm{g}}^{\star}$, $\mathrm{We}_{\mathrm{g}}^{\star}$ are based on boundary layer sizes

We=4000, Re=4000, r=0.1, m=0.025, We,Re based on domain size
Initial condition four vortices of circulation–si = 0.5, L–si=0.01

Fig. 7 Nonlinear development of the instability for the two viscosity methods and for two grid sizes (case E)

4.3 Ligament formation at balanced density

Before we move on to the solution of the full problem, it is interesting to consider a simpler case. We performed simulations with equal viscosity and densities, and a sharp velocity jump. Typical Kelvin–Helmholtz roll-ups are obtained, with the two phases occupying symmetrical regions of space. However if the base flow is made asymmetrical with a boundary layer in the gas only then the flow of Fig. 8 is observed. In that case, the boundary layer was linear as in Fig. 2b with no boundary layer in the liquid ($U_{\mathrm{l}} = 0$) and $\delta_{\mathrm{g}} = 0.2L$, $\mathrm{Re}_{\mathrm{l}} = \mathrm{Re}_{\mathrm{g}} = 2,000$, $\sigma = 0$. The grid size was 256×256 nodes. Notice how a ligament-like structure forms at $t = 1$. This demonstrates that density or viscosity asymmetry are not alone responsible for the asymmetric ligament formation: the asymmetry in boundary layers plays a major role. Such an asymmetry in boundary layers occurs in most realistic flows. As a result of the stress-balance condition (15) $U_{\mathrm{g}}/U_{\mathrm{l}} = \mu_{\mathrm{l}}/\mu_{\mathrm{g}}(\nu_{\mathrm{g}}/\nu_{\mathrm{l}})^{1/2}$. The right-hand side is a large number for most fluids, and thus most of the vorticity is in the gas.

4.4 Results for variable density

We have observed ligament formation and evolution in the nonlinear regime. Ligaments form if Re_{g}, We_{l} and Γ are all large enough, as shown in Fig. 9 (This diagram was completed at relatively low resolution, thus the results are not readily comparable to those of Figs. 11, 14, 17 etc.). A discussion of the limits in this diagram is given in the next section.

Four stages in the simulated development may be identified, although not all of them occur for all parameter values. (1) The interface deforms with a steadily growing amplitude. Vorticity remains attached close to the interface but the gas boundary layer grows more or less rapidly depending on the Reynolds number. This stage corresponds to the linear development of the instability as well as the early nonlinear development. (2) The vorticity detaches from the boundary layers. This corresponds to the situation at $t = 0.8$ in Fig. 8. (3) Ligaments form. In the symmetric fluids case this is the situation at $t = 1$. Various ligament shapes are shown in Figs. 11, 14, 17, 20, 21. (4) As the ligaments stretch and bend, their tips grow into a more or less visible bulge
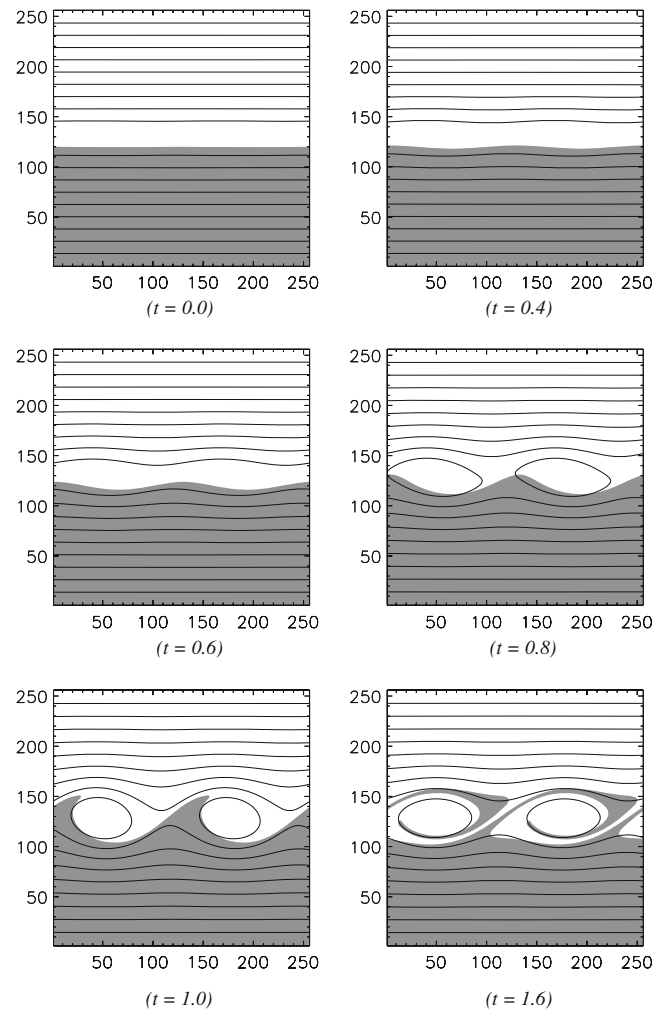
Fig. 8 Simulation of a sheared flow between identical fluids. There is no surface tension. The only asymmetry is in the boundary layers, as described in the text. The *lines* are streamlines and the *gray area* tracks what is considered to be the liquid phase. The gas boundary layer is visible as the region where streamlines are more sparse
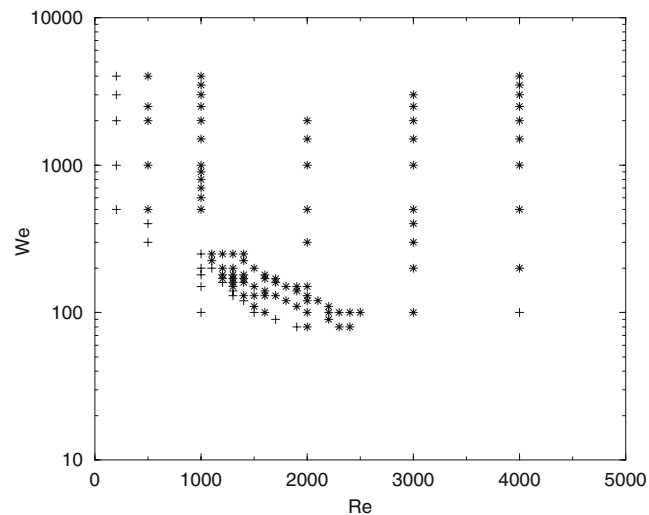
Fig. 9 Diagram in parameter space showing when ligaments form and eventually break at low (256 × 256) resolution. The ∗ symbols indicate that a ligament formed and broke, while the + symbols indicate that ligaments did not fully develop

or end rim from capillary effects. This rim is of the type studied by Taylor [31] and Culick [7]. It was shown by Brenner and Gueyffier [4] that it is more or less rounded depending on the ratio of viscous to surface tension forces. The 3D destabilization of this rim is one of the possible mechanisms for droplet formation [9].

A wider rim is most clearly seen when the Weber number is relatively moderate as in Fig. 11b. Behind the thick rim the ligament continues to stretch and eventually becomes so thin that it breaks. This rupture is a resolution-dependent phenomenon.

We have frequently observed between steps (2) and (3) that vortices merge, ending with a single ligament and a single vortical region. This vortex-merging phenomenon is consistent with the vortex merging observed in the spatial development of shear layers [5]. Indeed Raynal [25] has observed an increase in the wavelength with the distance from the nozzle. This overall picture is modified with the parameters of the flow in a way we shall now examine.

4.5 Effect of Reynolds and Weber numbers

Table 1 describes the cases simulated in the nonlinear regime. It contains four basic cases A, B, C and D and a few others derived from the basic cases. To build these cases, we consider two values of the gas Reynolds and Weber numbers: a small value of 500 and a large value of 4,000 and obtain four combinations. The growth rates predicted for five of the cases by the Orr–Sommerfeld theory are shown in Figs. 10, 13, 16, 19, and 22. These show the growth rate αc_i as a function of α, the wavenumber of the unstable mode; c_i is the imaginary part of the wave speed. The observed stability of the flow is however not immediately derived from the theoretical growth rates. This is because the base flow is not frozen as time increases, the boundary layer size increases as $\sqrt{\nu t}$. Thus an initially unstable configuration may become stable. The time scale for boundary layer growth for phase p is $t_\nu = \delta_p^2/\nu_p$ and the time scale for instability is $t_i = L\alpha c_i/\Delta U$. The ratio of the time scales is $R_p = t_\nu/t_i = \alpha c_i \mathrm{Re}_p^* \delta_p/L$, where Re_p^* is the Reynolds number based on boundary layer size and other quantities in phase p. To maintain the profile approximately frozen in both layers during the growth of the instability by several e-folds one needs to have both $R_g, R_1 >> 1$. A similar theory was put forward by Villermaux [32] and Raynal [25] but based on the inviscid linear theory alone. In the inviscid theory, there is only one unstable mode, which as a rule of thumb is less unstable than the viscous modes as shown by Boeck and Zaleski [3].

The lowest Re and We numbers are those of case A, for which simulations were performed with resolution up to 1024×1024. One sees from Table 1 and Fig. 10 that the $n' = 2$ mode, which corresponds to the initialization by our four vortices, is stable. However nonlinear interaction will also excite mode $n' = 1$ with wavenumber $\alpha = 2\pi$, which is barely unstable (Fig. 10) for which $R_g \simeq 0.4$. So despite the apparently high We and Re numbers for case A the conditions for instability are not met. Indeed case A lies just on the edge of the ligament-forming region in Fig. 9. Actually, case A is marked as "ligament-forming" in Fig. 9, which reports results at resolution 256×256 with a moderate initial perturbation ($\Gamma = 0.025$), while the sequence
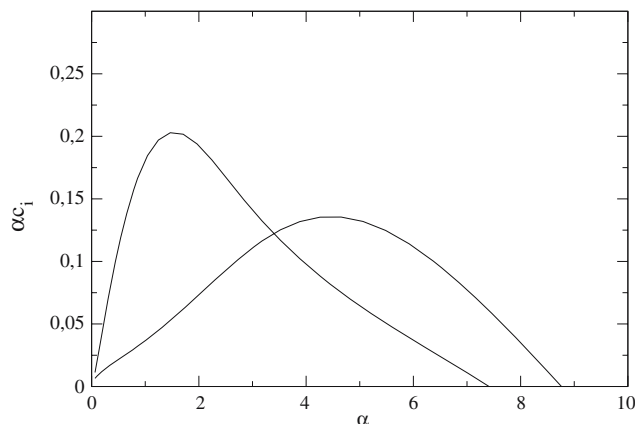
Fig. 10 The growth rates in linear Orr–Sommerfeld theory for case A. The wavenumber α is in units of $1/L$. Thus the wavenumbers that fit in the box are $\alpha = 2n'\pi$. Only the $n' = 1$ mode is unstable, while our initial condition with two pairs of vortices corresponds to $n' = 2$ and a stable mode. Both the standard mode and the H-mode are seen in this case

(a)

(b)
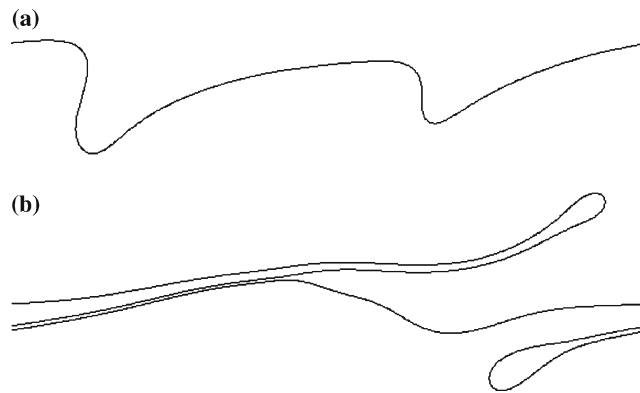
Fig. 11 Two stages of ligament formation and elongation at low Reynolds number, 512×512 grid, case A $\text{Re}_g = 500$ and $\text{We}_g = 500$, **a** $t = 2.8$, **b** $t = 7.92$

(a)

(b)
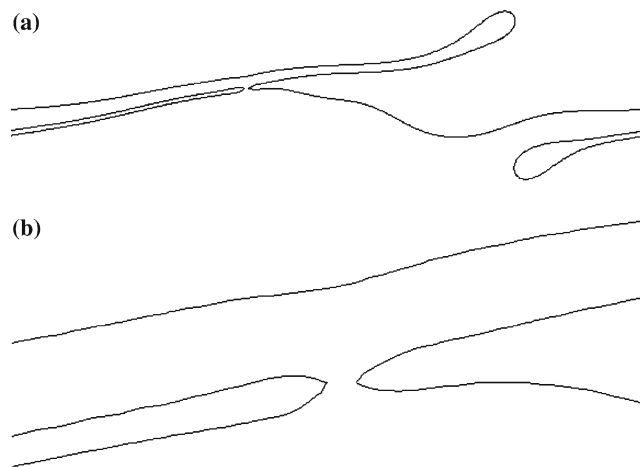
Fig. 12 Reconnection of the thin gas layer in simulation case A with filtered C in the surface tension method (Eq. 12), at time $t = 7.28$. **a** full domain, **b** detail

obtained at resolution 512×512 and higher with a similar moderate initial perturbation does not lead to fully formed ligaments and breakup.

It is interesting to notice that the instability in cases A and C would be even weaker, except for the existence of the second instability mode. This shows the importance of computing accurately the stability properties in the realistic viscous framework. Nonlinear calculations show that ligaments form in a transient way but subsequently do not stretch sufficiently to eventually fracture, even at moderate resolution. However, with a relatively large circulation in the initial condition ($\Gamma = 0.075$), one does see the formation of a ligament, with a relatively large end rim. For such a large initial circulation the early nonlinear shapes differ from those obtained with smaller amplitude vortices (for instance in Fig. 6). The air forms fingers that enter the liquid (Fig. 11a). An interesting effect of the surface-tension algorithm may be observed. In Fig. 12 we see that using the filtered C for surface tension creates an attractive force between the interfaces that speeds up the reconnection. This may be understood as the filtering will *feel* the neighboring interface at a longer distance. In some sense it makes the interface thicker from the point of view of the surface-tension method. Without filtering, a similar reconnection also occurs but much later, at $t = 8.8$.

Case C has the same moderate Re but larger We. A thinner, longer ligament is created (Fig. 14), at the standard value of the circulation. We show in Fig. 14c the last image before reconnection occurs: in a manner similar to case A, the thin air film reconnects.
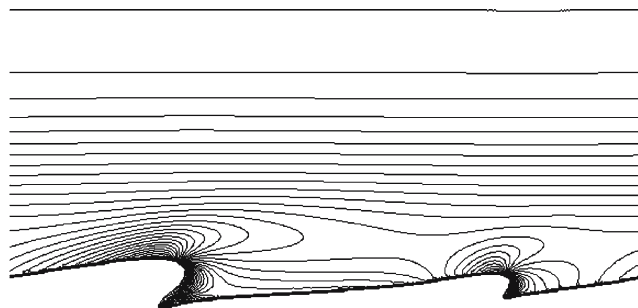
If we increase the Reynolds number but keep the Weber number moderate as in case B we obtain the sequence shown in Fig. 17. It is seen that the two bumps merge between times $t = 4$ and $t = 4.8$. At $t = 9.76$, just before breakup a very long ligament is seen (the reader should remember that the domain is periodic, and lines ending on the right are connected to lines starting on the left; thus in Fig. 17c a single ligament winds
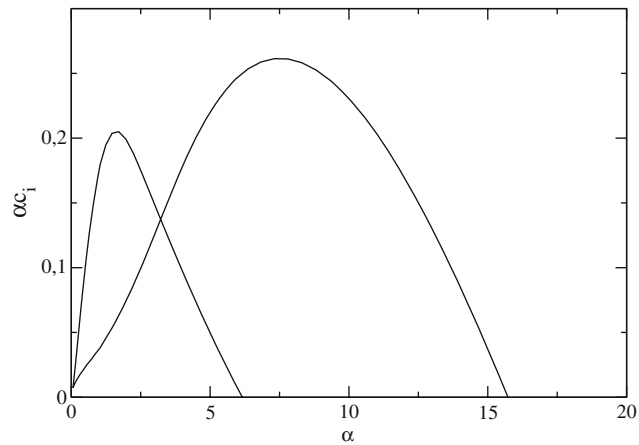
Fig. 13 The growth rates in linear Orr–Sommerfeld theory for case C. Two modes are seen again

Fig. 14 Three stages of ligament formation and elongation at low Reynolds number, 512×512 grid, case C Re $_g = 500$ and We $_g = 4,000$, **a** $t = 4$, **b** $t = 5.6$, **c** $t = 8.8$


Fig. 15 Vorticity in case C at $t = 4$

around the periodic box). The complex shape observed at time 9.76 is created by a process of folding and stretching.

Finally, if we increase the Reynolds number and the Weber number as in case D the ligament folds again in complex ways, as shown in Fig. 20.

The effect of the gas Reynolds number on the stretching and fracture mechanism can be seen by comparing the results for the low Reynolds number cases A and C with those of the higher Reynolds numbers cases B and D. At relatively low Reynolds number (near the left boundary in Fig. 9) the boundary layer $\delta_g(t)$ grows fast. Before the ligaments have fully developed, the boundary layer has spread over the entire box and little vorticity is left. This may be seen in Fig. 15 which shows the vorticity contours for case C. At higher Reynolds number, the vorticity does not spread but detaches from the ligaments as shown in Fig. 18. This process of boundary layer separation, or roll-up, may occur very early. At high Reynolds numbers even a small deformation of the interface triggers separation and roll up.
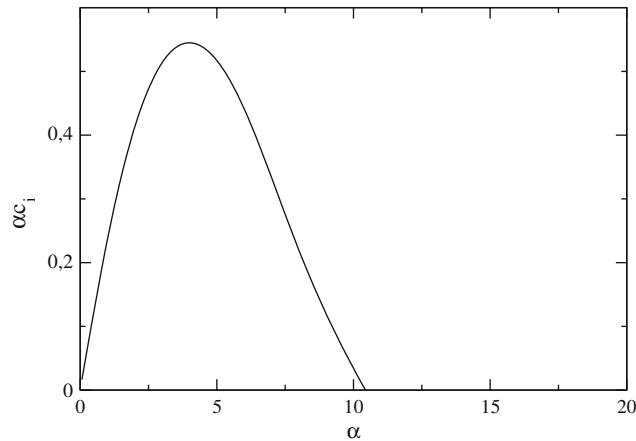
Fig. 16 The growth rates in linear Orr–Sommerfeld theory for case B
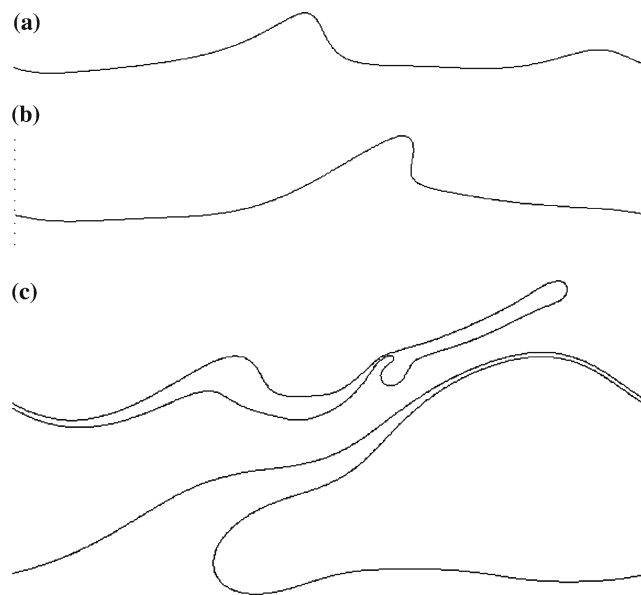
Fig. 17 Three stages of ligament formation and elongation at higher Reynolds number, 512×512 grid, case B: $Re_g = 4,000$ and $We_g = 500$, **a** $t = 4$, **b** $t = 4.8$, **c** $t = 9.76$

The effect of the Weber number may also be inferred from these results. As a rough guide, a large Weber number favors the formation of very thin ligaments with almost negligible end rims. However the time at which the ligament is observed is also relevant. When breakup occurs late, ligaments had the time to thin in their central part but the end rims have grown. This may be seen for instance in Fig. 14c; although the Weber number is rather large, a significant end rim is seen.

4.6 The effect of the perturbation amplitude

One effect of a large perturbation amplitude has already been seen in case A: the air penetrates the liquid.

In the high-Reynolds-number case, varying the initial amplitude of the perturbation also has a dramatic effect on the fate of the ligament. Increasing the initial perturbation, as in Case D1, makes the ligament rapidly sprout up. A thin ligament, pointing upwards, is formed. It is shown just before its breakup (at time $t = 4$) in Fig. 21.

The amplitude for initial perturbations that is realistic depends on the experiment or natural configuration being considered. While some nozzles will involve highly turbulent flow, others are controlled to reduce the

(a)

(b)
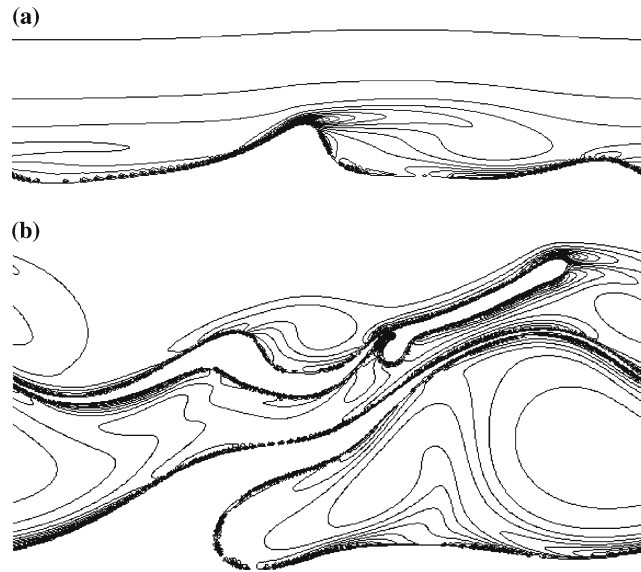
**Fig. 18** Vorticity in case B at **a** $t = 4$ and **b** $t = 9.76$
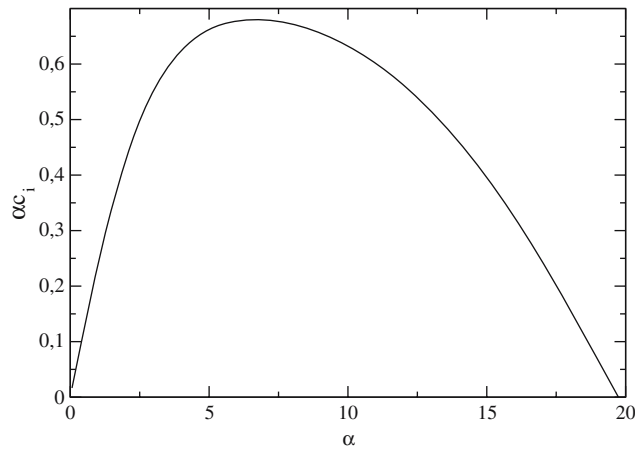
Fig. 19 The growth rates in linear Orr–Sommerfeld theory for case D

level of turbulence in the nozzle. The turbulence level, defined as the ratio of the root-mean-square fluctuating velocity to the mean flow velocity, may arguably be of the order of Γ, and turbulence levels of 0.01 are not uncommon.

4.7 Effect of the boundary layers

All the simulations we have shown so far involve boundary layers of the shape shown in Fig. 2c, obey the condition of diffusive growth of the boundary layers (14) and have the same width in the gas layer. We have attempted many simulations where one or several of these conditions are modified. This usually changes the eventual fate of the ligament. For instance, thinner boundary layers change case D1, in which the ligament was pointing upwards before breakup, into ligaments rolling downwards (Fig. 23). The result for these thin boundary layers is however different from the result obtained with no boundary layers (case E, not shown for late times).

Finally we have attempted to simulate the kind of boundary layers that would occur just downstream of the splitter plate between parallel liquid and gas streams. In that case, just behind the splitter plate, the boundary
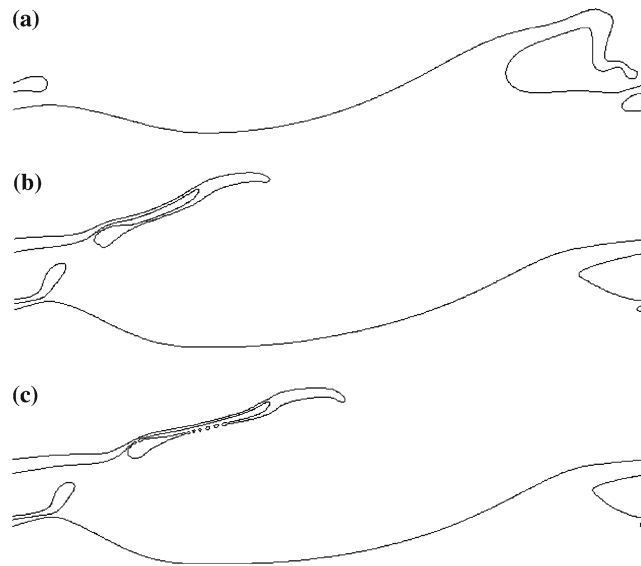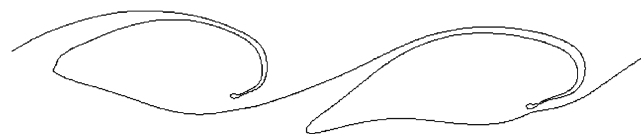
Fig. 20 Three stages of ligament formation and elongation at higher Reynolds number, 512×512 grid, case D $Re_g = 4,000$ and $We_g = 4,000$, **a** $t = 6$, **b** $t = 6.8$, **c** $t = 6.96$

Fig. 21 Case D1 (the same as D but at a larger perturbation amplitude): the breakup occurs much earlier, just after time $t = 4$, which is shown here
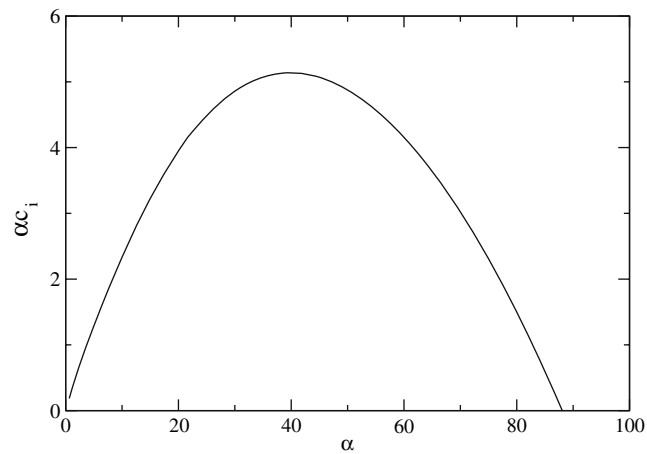
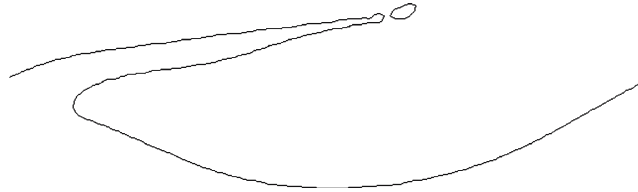**Fig. 22** The growth rates in linear Orr–Sommerfeld theory for case D2

Fig. 23 Case D2: larger perturbation amplitude but thinner boundary layers. At time $t = 2.4$ the ligaments roll up instead of shooting upwards

Fig. 24 Case D3: inverted liquid boundary layer. At time $t = 4.48$ the left ligament points up and is about to break

Fig. 25 Case B at lower resolution: the breakup occurs much earlier than in the high-resolution case. Here the ligament is shown at $t = 8.4$ just before breakup

layers will have the shape shown in Fig. 2d. In case D3 the liquid velocity is now of the opposite sign

$$u_{0,1}(y) = -U_1\text{erf}\left(\frac{y}{\delta_1}\right). \tag{16}$$

In case D3, the parameters are identical to case D but the condition of stress balance (15) cannot be verified. The liquid velocity is instead set arbitrarily by $U_1/U_g = 0.1$ (a realistic ratio for laboratory experiments). We now find again a ligament pointing rapidly upwards (Fig. 24).

4.8 Effect of grid resolution

One effect of grid resolution that we have already reported is that coarse grids lead to stronger instability: for instance in case A ligaments form at 256×256 as shown in Fig. 9 while ligaments do not form at higher resolution. This is due to a lower effective surface tension at low resolution. Once instability is set and ligaments are stretching, finer grids lead to later breakups, however the process is not uniform. At some moments and locations in the flow, the ligaments are caught in rapid elongational flows that break them rapidly no matter what the resolution. Then increasing the resolution has no dramatic effect. For most of the figures shown, varying the resolution between 256^2 and 1024^2 has no qualitative effect. On the other hand, in some cases a remarkable effect is seen. In Fig. 25 we show case B at low resolution, just before breakup. In a sense, this lower-resolution simulation may look more realistic compared to experimental photographs: this may be because the thinner, longer, convoluted ligaments obtained at larger resolution are often broken by three-dimensional effects.

5 Conclusion

We have described a method built on several known numerical schemes, such as VOF, which together allow the deformation of interfaces in a mixing layer to be followed. The validation is performed through comparisons with the linear theory. In this way a kind of cross-validation is achieved: the linear theory, which is rather complex, is also made more reliable through the agreement with the full numerical resolution of the Navier–Stokes equations.

We also show that the method used to approximate the viscous terms in the mixed cells may have an important effect on the growth rate, but the effect is limited to the range where the perturbation amplitude is small relative to the grid size. Nevertheless, this effect may over-amplify the growth of some length scales if proper care is not taken.

Indeed, our results show that one ingredient of a careful treatment of the instability is the introduction of boundary layers in the initial conditions. The absence of initial boundary layers makes the problem ill-posed because of the appearance of rapidly growing modes. This results in poor convergence as the grid is refined.

On this basis we have been able to obtain some results on the nonlinear development of the instability. One of the most striking effects is that relatively large Reynolds and Weber numbers are necessary to observe

growing ligaments. Going further in time after the formation of the ligaments, one eventually sees the topology of the solutions change. This event is dependent on the grid resolution and thus difficult to analyze. Physical reality is three-dimensional and because of this the real flows may diverge from the solutions in this paper before the breakup stages we have identified actually occur. On the other hand, in a fast flow the width of the sheets may become so thin, of the order of nanometers, that they would break physically (see Raynal [25], pp. 196 and 198 for experimental evidence).

Nevertheless the simulations show realistic mechanisms and may be used to build theories of droplet formation. A systematic prediction of the size of the end rim may help to determine the final droplet size. As seen in this paper, accurate predictions require very-high-resolution simulations. A complete series of such simulations should be undertaken to determine end-rim size as a function of the physical parameters.

Another perspective of this work is to perform three-dimensional and spatially developing simulations of comparable resolution. Most existing three-dimensional work, including the work by some of us (for instance [2,35]) suffers from one or several defects that we tried to avoid in the present work: resolution too small (i.e., grids too coarse), initial perturbation amplitude too large, lack of boundary layers. Correcting these defects is likely to require extensive computing resources, even allowing for a future marked increase in computer power.

Another perspective is to extend these results to more realistic cases, where the parameters are closer to the experimental conditions of an air–water experiment in a laboratory or a wind-generated wave in the natural environment. Such a study would involve more numerical difficulties than the present one, as it requires increases in both the surface tension (or the Laplace number) and the density ratio. It would however be of considerable interest.

References

1. Aulisa, E., Manservisi, S., Scardovelli, R., Zaleski, S.: A geometrical area-preserving volume of fluid method. J. Comput. Phys. **192**, 355–364 (2003)
2. Bianchi, G.M., Pelloni, P., Toninel, S., Scardovelli, R., Leboissetier, A., Zaleski, S.: A quasi-direct 3D simulation of the atomization of high-speed liquid jets. In: Proceedings of ICES05, 2005 ASME ICE Division Spring Technical Conference. Chicago, Illinois, April 5–7, 2005
3. Boeck, T., Zaleski, S.: Viscous versus inviscid instability of two-phase mixing layers with continuous velocity profile. Phys. Fluids **17**, 032106 (2005)
4. Brenner, M., Gueyffier, D.: On the bursting of viscous films. Phys. Fluids **11**, 737–739 (1999)
5. Brown, G.L., Roshko, A.: On density effects and large structure in turbulent mixing layers. J. Fluid Mech. **64**, 775–816 (1974)
6. Chandrasekhar, S.: Hydrodynamic and Hydromagnetic Stability. Oxford University Press, Oxford (1961)
7. Culick, F.E.C.: Comments on a ruptured soap film. J. Appl. Phys. **31**, 1128–1129 (1960)
8. Faeth, G., Hsiang, L.-P., Wu, P.-K.: Structure and breakup properties of sprays. Int. J. Multiphase Flow **21**, 99–127, supplement issue (1995)
9. Fullana, J.M., Zaleski, S.: Stability of a growing end-rim in a liquid sheet of uniform thickness. Phys. Fluids **11**, 952–954 (1999)
10. Gordillo, J.M., Perez-Saborid, M.: On the first wind atomization regime. J. Fluid. Mech. **541**, 1–20 (2005)
11. Gueyffier, D., Nadim, A., Li, J., Scardovelli, R., Zaleski, S.: Volume of fluid interface tracking with smoothed surface stress methods for three-dimensional flows. J. Comput. Phys. **152**, 423–456 (1999)
12. Hinch, E.: A note on the mechanism of the instability at the interface between two shearing fluids. J. Fluid Mech. **144**, 463–465 (1984)
13. Hooper, A.P.: Long-wave instability at the interface between two viscous fluids: thin layer effects. Phys. Fluids **28**(6), 1613–1618 (1985)
14. Hooper, A.P., Boyd, W.G.C.: Shear-flow instability at the interface between two viscous fluids. J. Fluid Mech. **128**, 507–528 (1983)
15. Hooper, A.P., Boyd, W.G.C.: Shear-flow instability due to a wall and a viscosity discontinuity at the interface. J. Fluid Mech. **179**, 201–226 (1987)
16. Hoyt, J.W., Taylor, J.: Waves on water jets. J. Fluid Mech. **83**, 119–127 (1977)
17. Keller, F.X., Li, J., Vallet, A., Vandromme, D., Zaleski, S.: Direct numerical simulation of interface breakup and atomization. In: Yule, A.J. (ed.) Proceedings of ICLASS94, pp. 56–62. Begell House, New York (1994)
18. Lafaurie, B., Nardone, C., Scardovelli, R., Zaleski, S., Zanetti, G.: Modelling merging and fragmentation in multiphase flows with SURFER. J. Comput. Phys. **113**, 134–147 (1994)
19. Lasheras, J.C., Hopfinger, E.J.: Liquid jet instability and atomization in a coaxial gas stream. Annu. Rev. Fluid Mech. **32**, 275–308 (2000)

20. Leboissetier, A., Zaleski, S.: Influence des conditions amont turbulentes sur l'atomisation primaire. Combustion (Revue des Sciences et Techniques de Combustion) **2**, 75–87 (2002)
21. Lefebvre, A.H.: Atomization and Sprays. Taylor & Francis, London (1989)
22. Li, J.: Calcul d'interface affine par morceaux (piecewise linear interface calculation). C. R. Acad. Sci. Paris, série IIb, (Paris) **320**, 391–396 (1995)
23. Marmottant, P., Villermaux, E.: Atomisation primaire dans les jets coaxiaux. Combustion (Revue des Sciences et Techniques de Combustion) **2**, 89–126 (2002)
24. Rangel, R., Sirignano, W.: Nonlinear growth of Kelvin–Helmholtz instability: effect of surface tension and density ratio. Phys. Fluids **31**, 1845–1855 (1988)
25. Raynal, L.: Thèse. PhD thesis, Universite Joseph Fourier, Grenoble (1997)
26. Reitz, D., Bracco, F.: Mechanism of atomisation of a liquid jet. Phys. Fluids **25**, 1730–1742 (1982)
27. Scardovelli, R., Zaleski, S.: Direct numerical simulation of free-surface and interfacial flow. Annu. Rev. Fluid Mech. **31**, 567–603 (1999)
28. Scardovelli, R., Zaleski, S.: Interface reconstruction with least-square fit and split Lagrangian-Eulerian advection. Int. J. Numer. Meth. Fluids **41**, 251–274 (2003)
29. Tauber, W., Tryggvason, G.: Direct numerical simulation of primary breakup. Comput. Fluid Dyn. J. **9**, 158 (2000)
30. Tauber, W., Unverdi, S.O., Tryggvason, G.: The non-linear behavior of a sheared immiscible fluid interface. Phys. Fluids **14**, 2871 (2002)
31. Taylor, G.I.: The dynamics of thin sheets of fluid III. Disintegration of fluid sheets. Proc. Roy. Soc. Lond. A **253**, 313–321 (1959)
32. Villermaux, E.: On the role of viscosity in shear instabilities. Phys. Fluids **10**, 368–373 (1998)
33. Yecko, P., Zaleski, S., Fullana, J.-M.: Viscous modes in two-phase mixing layers. Phys.Fluids **14**, 4115–4122 (2002)
34. Zaleski, S., Li, J., Scardovelli, R., Zanetti, G.: Flows with interfaces: dealing with surface tension and reconnection. In: Proceedings of the IMACS-COST Conference on Computational Fluid Dynamics, Lausanne Sept. 13–15, 1995. Notes on Numerical Fluid Mechanics, p. 53. Vieweg, Braunschweig (1995)
35. Zaleski, S., Li, J., Scardovelli, R., Zanetti, G.: Direct simulation of multiphase flows with density variations. In: IUTAM colloquium "Variable Density Low Speed Turbulent Flows". Kluwer, Dordrecht (1996)